Journal of
Applied Physics

RESEARCH ARTICLE | JUNE 11 2024

Analysis of local strain fields around individual threading dislocations in GaN substrates by nanobeam x-ray diffraction

T. Hamachi ; T. Tohei ; Y. Hayashi ; S. Usami ; M. Imanishi; Y. Mori; K. Sumitani; Y. Imai ;
S. Kimura ; A. Sakai

J. Appl. Phys. 135, 225702 (2024)
https://doi.org/10.1063/5.0199961

Journal of
Applied Physics
ARTICLE
pubs.aip.org/aip/jap

Analysis of local strain fields around individual threading dislocations in GaN substrates by nanobeam x-ray diffraction

Cite as: J. Appl. Phys. **135**, 225702 (2024); doi: 10.1063/5.0199961
Submitted: 24 January 2024 · Accepted: 23 May 2024 ·
Published Online: 11 June 2024

T. Hamachi,[1,a)] T. Tohei,[1,b)] Y. Hayashi,[1,c)] S. Usami,[2] M. Imanishi,[2] Y. Mori,[2] K. Sumitani,[3] Y. Imai,[3] S. Kimura,[3] and A. Sakai[1,b)]

AFFILIATIONS

[1] Graduate School of Engineering Science, Osaka University, 1-3 Machikaneyama-cho, Toyonaka, Osaka 560-8531, Japan
[2] Graduate School of Engineering, Osaka University, 2-1 Yamadaoka, Suita, Osaka 565-0871, Japan
[3] Diffraction and Scattering Division, Japan Synchrotron Radiation Research Institute (JASRI), 1-1-1 Koto, Sayo, Hyogo 679-5198, Japan

[a)] **Electronic mail:** u679849k@alumni.osaka-u.ac.jp
[b)] **Author to whom correspondence should be addressed:** tohei@ee.es.osaka-u.ac.jp and sakai@ee.es.osaka-u.ac.jp
[c)] **Present address:** National Institute for Materials Science, 1-2-1 Sengen, Tsukuba, Ibaraki, 305-0047, Japan

ABSTRACT

Position-dependent three-dimensional reciprocal space mapping (RSM) by nanobeam x-ray diffraction (nanoXRD) was performed to reveal the strain fields produced around individual threading dislocations (TDs) in GaN substrates. The distribution and Burgers vector of TDs for the nanoXRD measurements were confirmed by prerequisite analysis of multi-photon excited photoluminescence and etch pit methods. The present results demonstrated that the nanoXRD can identify change in the lattice plane structure for all types of TDs, i.e., edge-, screw-, and mixed TDs with the Burgers vector of $\mathbf{b} = 1\boldsymbol{a}$, $1\boldsymbol{c}$ and $1\boldsymbol{m} + 1\boldsymbol{c}$. Strain tensor components related to edge and/or screw components of the TDs analyzed from the three-dimensional RSM data showed a nearly symmetrical strained region centered on the TD positions, which were in good agreements with simulation results based on the isotropic elastic theory using a particular Burgers vector. The present method is beneficial in that it allows non-destructive analysis of screw components of TDs that tend to contribute to leakage characteristics and are not routinely accessible by conventional structural analysis. These results indicate that nanoXRD could be a powerful way to reveal three-dimensional strain fields associated with arbitrary types of TDs in semiconductor materials, such as GaN and SiC.

I. INTRODUCTION

Wide-bandgap semiconductor materials based power devices, such as silicon carbide (SiC) and gallium nitride (GaN), are undergoing widespread implementation in industrial applications, such as automotive cars.[1–4] Commercially available wafers of these types of materials still contain threading dislocations (TDs), and their densities typically range from 10^3 to $10^4\,\mathrm{cm}^{-2}$ for SiC and 10^3–$10^6\,\mathrm{cm}^{-2}$ for GaN. Such a high density of the dislocations, especially for GaN, extended defects, and dislocation reactions (coalescence and branch of dislocations) are quite common, which are closely associated with residual strains and plasticity of as-grown crystals, leading to wafer-scale problems, such as bowing and clacks. Residual TDs in substrates can be detrimental to device properties: reduction of on-resistance,[5] reverse leakage current path,[6–8] and scattering carriers resulting in a reduction of the mobility.[9,10] Electrical and electronic behaviors of the dislocations could vary as a result of segregation and diffusion of impurities along the dislocations,[11,12] and elastic strain fields generated by dislocations themselves would have an essential role of interaction with the impurities.[13,14] Understanding the nature of dislocations, including the strain fields, allows us to better develop novel methods for producing high-performance power devices.

Typical TDs propagating to the *c*-direction in SiC and GaN have Burgers vector of $\mathbf{b} = 1/3\langle 11\bar{2}0\rangle = 1\boldsymbol{a}$, $\mathbf{b} = \langle 0001\rangle = 1\boldsymbol{c}$, and $\mathbf{b} = 1/3\langle 11\bar{2}3\rangle = 1\boldsymbol{a} + 1\boldsymbol{c}$, which are generally classified into three categories: edge, screw, and mixed-types, while some unique mixed TDs having relatively larger Burgers vectors, such as $\mathbf{b} = \mathrm{n}\boldsymbol{a} + 1\boldsymbol{c}$ (n = 2 and 3) and $\mathbf{b} = \langle 1\bar{1}01\rangle = 1\boldsymbol{m} + 1\boldsymbol{c}$, were also reported.[7,15–18] There are several techniques to measure the residual strain. Geometric phase analysis (GPA) based on a high-resolution transmission electron microscope (TEM) enables to analyze strain fields around a core of dislocations in an atomic scale,[19] but the strain around screw dislocations not generating in-plane displacement cannot be basically analyzed. Large-angle convergent-beam electron diffraction (LACBED) using TEM has the advantage of determination of an absolute value of the Burgers vector of dislocations,[6–8,15–18] though quantitative analysis of strain fields around the dislocation is difficult. In the TEM-based analysis, there are also concerns about damages due to the TEM sample processing and strain relaxation due to thinning the sample. Raman spectroscopy and x-ray topography are nondestructive techniques to evaluate the strain and characterize types of TDs. Raman shift mapping can reveal the in-plane strain of the edge component of pure edge and mixed TDs in GaN.[20,21] However, this technique does not detect the strain around a screw component of TDs due to the same reason as the GPA mentioned above. In synchrotron radiation x-ray topography, intensity of a diffracted x ray from a specific Bragg plane is recorded and all types of TDs can be sensitively characterized as a contrast variation in topographic images depending on the Burgers vector,[22,23] but the strain fields around the TDs cannot be quantified.

Nanobeam x-ray diffraction (nanoXRD) measurement using the incident x ray focused to several-hundred nm in diameter with high-brilliance synchrotron sources is an attractive method to evaluate microlattice plane structure in crystals due to its penetrative nature for various semiconductor materials.[24–27] Position-dependent three-dimensional reciprocal space (ω–2θ-φ) mapping, which can detect local lattice tilt and twist and lattice constant in the crystals, has a potential to reveal microstrain fields in the vicinity of individual TDs. Previously, we investigated three-dimensional variations in the lattice microstructure along a growth direction in nitride semiconductor crystals by nanoXRD.[24,25] The results clarify modulations in the lattice plane tilt, twist, and spacing originated from a shift in crystal growth modes, specific void configurations formed at an interface of the epitaxial layers and substrates, and propagation of dislocations.[24,25] In this study, the nanoXRD technique is used to reveal the microstrain induced by individual TDs in GaN bulk crystals with a high spatial resolution. By comparing in-plane $\omega-2\theta-\varphi$ mapping by nanoXRD with the distribution and the type (i.e., Burgers vector) of TDs observed by a combination of multi-photon excited photoluminescence (MPPL) and etch pit methods, modulation in the lattice plane structure around all types of TDs can be identified. The strain fields of the edge and screw components of the TDs analyzed from the $\omega-2\theta-\varphi$ data are quantitatively discussed based on simulation results by isotropic elastic theory of dislocations.

II. EXPERIMENTAL

The Si-doped thick GaN layer over 200 μm was homoepitaxially grown by hydride vapor epitaxy on a Na-flux-grown substrate.[28] The surface of the HVPE-GaN was smoothed by chemical–mechanical polishing (CMP). Wet chemical etching with a eutectic mixture of sodium hydroxide and potassium hydroxide at 450 °C for 20 min was conducted to make TD-related etch pits on a surface of the sample. As reported in our previous study on the same type HVPE-GaN crystals, sizes of the etch pits were correlated with the Burgers vector of the TDs: TDs having $\mathbf{b} = 1/3\langle 11\bar{2}0\rangle$, $\mathbf{b} = 1/3\langle 11\bar{2}3\rangle$, $\mathbf{b} = \langle 0001\rangle$, and $\mathbf{b} = \langle 1\bar{1}01\rangle$ formed extra small (XS), small, medium (M), and large (L) pits, respectively.[16] Figures 1(a) and 1(b) present scanning electron microscopy images of two different surface areas referred to as area1 and area2, respectively (taken by an FEI Versa3D dual beam system at an acceleration voltage of 5 kV). The area1 contains one L- and several XS-sized etch pits and the area2 contains one M- and several XS-sized etch pits. Thus, we expected that a mixed TD with $\mathbf{b} = \langle 1\bar{1}01\rangle$ and edge TDs with $\mathbf{b} = 1/3\langle 11\bar{2}0\rangle$ existed in the area1 while a screw TD with $\mathbf{b} = \langle 0001\rangle$ and edge TDs with $\mathbf{b} = 1/3\langle 11\bar{2}0\rangle$ in the area2. Then, the surface was polished by several micrometers via CMP again to remove the etch pit. To locate dislocation positions for nanoXRD experiments, we performed MPPL observations (Nikon A1MP instrument with an excitation laser wavelength of 800 nm and a PL detection range of 352–388 nm). As indicated in Figs. 1(c) and 1(d) showing the MPPL images, it was confirmed that the locations of the threading dislocations coincided with those of the etch pits. Figures 1(e) and 1(f) show MPPL images at the depth of 9.3 μm in the area1 and area2, and the dislocations' spots at the surface are indicated by the dots. From the positional shifts of the dislocation's spots between the surface and the 9.3 μm depth, we can estimate inclination angles of the dislocations. The inclination angles of the edge, screw, and mixed dislocations in these regions were estimated to be 3.9°, 3.8°, and 2.4° at most, respectively, indicating propagation almost parallel to the [0001] axis within a penetration depth of the x-ray beam of 9.1 μm.

To analyze the strain fields in the vicinity of each TD, the position-dependent reciprocal space mapping (RSM) within the area1 and area2 by a nanoXRD technique was performed at the hard x-ray undulator beamline (BL13XU) in SPring-8. The primary x-ray beam having a photon energy of 8 keV monochromatized by a Si (111) double-crystal monochromator was focused by a zone plate. The beam size was 480 (vertical) × 770 nm^2 (horizontal) for the area1 and 370 (vertical) × 820 nm^2 (horizontal) for the area2 measurements. The angular divergence of the incident beam was estimated to be 0.029°. The diffracted x rays were detected by a two-dimensional hybrid pixel array detector (HyPix-3000, Rigaku Corp.) with a pixel size of 100 μm. The distance between the detector and the GaN sample was 1000.9041 mm. The resolution of 2θ and φ was calculated to be $5.72 \times 10^{-3°}$. The detailed optical setup of a nanoXRD measurement has been described in Refs. 27 and 29. The diffraction geometry for the nanoXRD measurement in this study is schematically presented in Fig. 2(a). The x ray was irradiated in the direction parallel to $[11\bar{2}0]$ of the GaN crystal. Symmetric 0004 and asymmetric $11\bar{2}4$ planes were selected as Bragg reflection planes. The footprint sizes of the incident x-ray beam in the horizontal direction for the 0004 and $11\bar{2}4$ reflection were 1280 and 770 nm for the area1 measurement and 1366 and 820 nm for the area2 measurement, respectively. Penetration depth

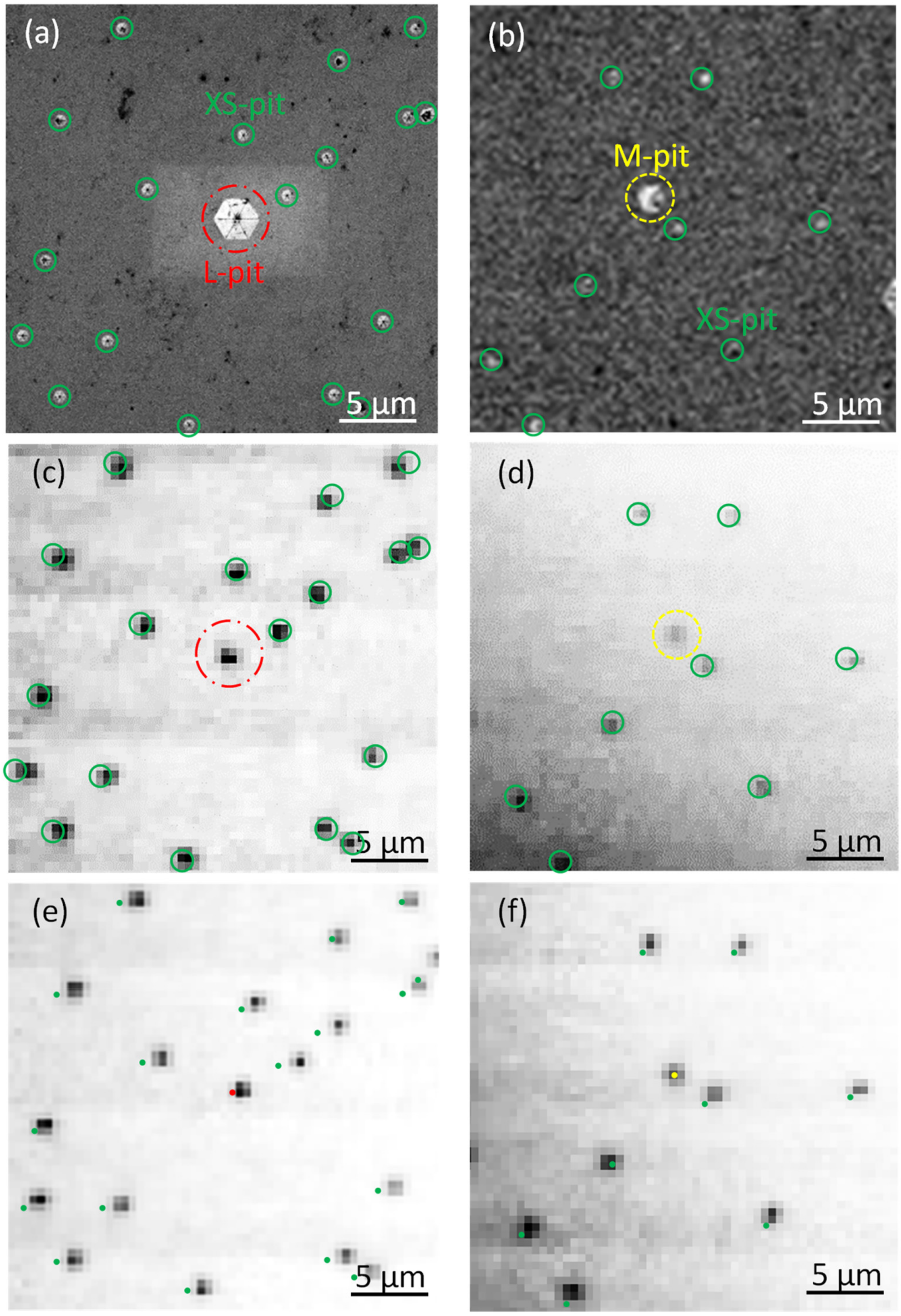

FIG. 1. Scanning electron microscopic images of (a) area1 and (b) area2 after the chemical etching. (c)–(f) MPPL images of (c) and (e) area1, and (d) and (f) area2 after removing the etch pits by CMP. (c) and (d) are observed at the surface, while (e) and (f) are at the depth of 9.3 μm from the surface. In (a)–(d), the L-pit, M-pit, and XS-pits are indicated by circles with red dashed, yellow broken, and green solid lines. In (e) and (f), dark spot positions (corresponding to the nonradiative spot due to the TD) at the surface seen in (c) and (d) are marked by dots using the same color as in (a)–(d).

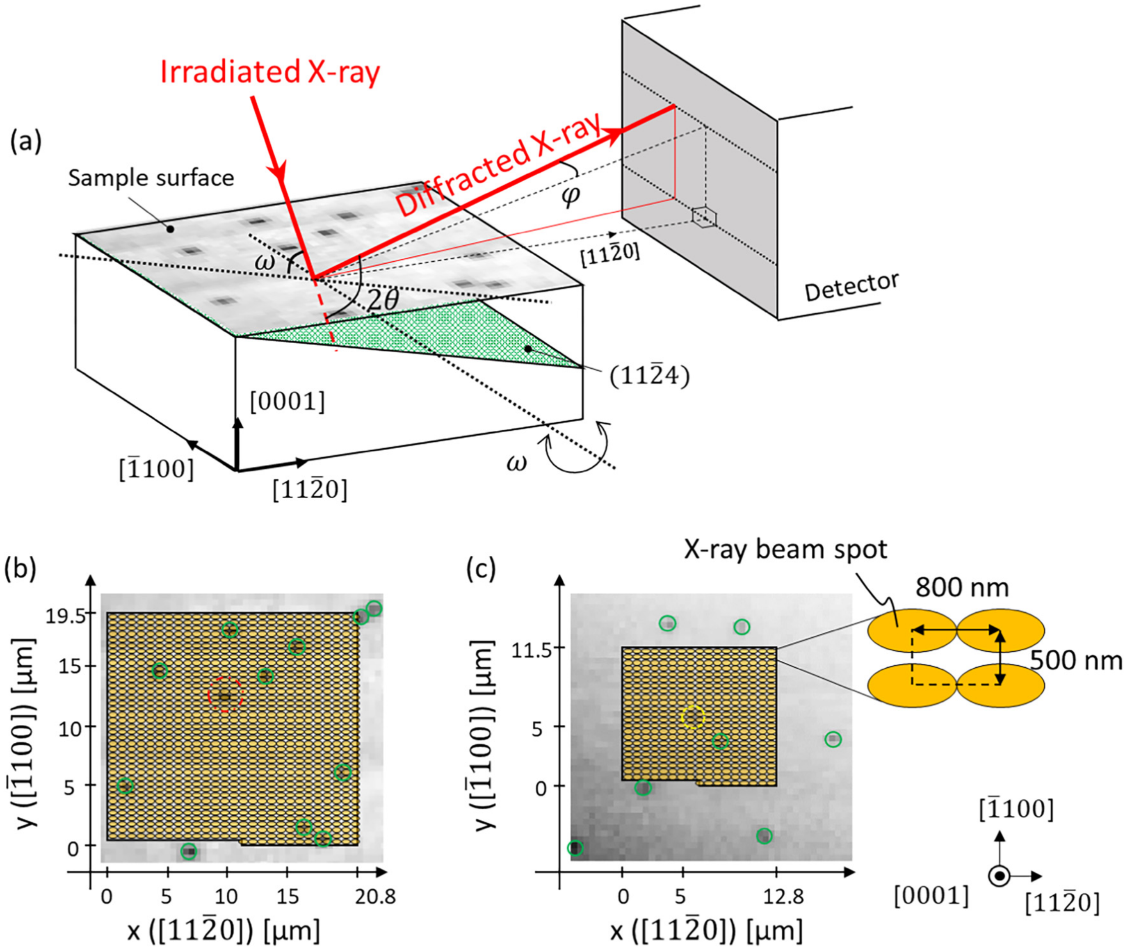

FIG. 2. (a) A schematic diagram of nanoXRD geometry and position-dependent ω–2θ–φ mapping for (b) area1 and (c) area2. In (b) and (c), the irradiated spots of the x-ray beam are superimposed on the corresponding surface MPPL images with the TD spots indicated by the same-colored circles as in Figs. 1(c) and 1(d).

of the x-ray beam in the GaN crystal is estimated to be approximately 9.1 and 5.0 μm in the case of the 0004 and $11\bar{2}4$ reflection, respectively. The incident beam was scanned on the GaN surface at the 800 and 500 nm steps along [$11\bar{2}0$] and [$\bar{1}100$] directions over 20.8×19.5 and $12.8 \times 11.5\,\mu\text{m}^2$ for areas 1 and 2, respectively, so that the scanned area1 included one L- (mixed dislocation) and several XS-pits (edge dislocations) and the area2 included one M- (screw dislocation) and one XS-pits (edge dislocation), as shown in Figs. 2(b) and 2(c). The lattice plane tilt, spacing, and twist in the GaN crystal are associated with ω, 2θ, and φ, respectively, as described in Fig. 2(a). Diffraction intensity spots acquired by ω–2θ–φ mapping from respective measurement positions generally have a finite broadening in each angular direction due to imperfect crystallinity of GaN. By the same data processing as reported in our previous study,[25] three profiles of intensity vs ω, 2θ, and φ were obtained from the raw ω–2θ–φ data, and lattice plane tilt (Ω), scattering angle (2Θ) corresponding to lattice spacing, lattice plane twist (Φ), and each fluctuation ($\Delta\omega$, $\Delta 2\theta$, and $\Delta\varphi$) were calculated from the center and the full width at half maximum of Gaussian fitting of the respective profiles. By extracting their values from ω–2θ–φ data for all measurement points in the area1 and area2, in-plane distributions of lattice plane microstructure could be evaluated.

III. RESULTS AND DISCUSSION

Figures 3(a)–3(f) present two-dimensional maps of Ω, 2Θ, Φ, $\Delta\omega$, $\Delta 2\theta$, and $\Delta\varphi$ in the area1, respectively. The circles indicating TD spots at the surface are arranged at the same positions as in Figs. 1(a) and 1(c). In Figs. 3(a)–3(c), it can be found that Ω, 2Θ, and Φ values largely and sharply change around the L-pit region compared to those in other regions. The local modulations of the lattice structure around the L-pit were confirmed in the $\Delta\omega$, $\Delta 2\theta$, and $\Delta\varphi$ maps in Figs. 3(d)–3(f). The degree of the modulation around the XS-pits is comparatively small and apparently unclear in Figs. 3(a)–3(c), but recognized sensitively in the $\Delta\omega$, $\Delta 2\theta$, and $\Delta\varphi$ maps in Figs. 3(d)–3(f). Strains of XS-pits show some

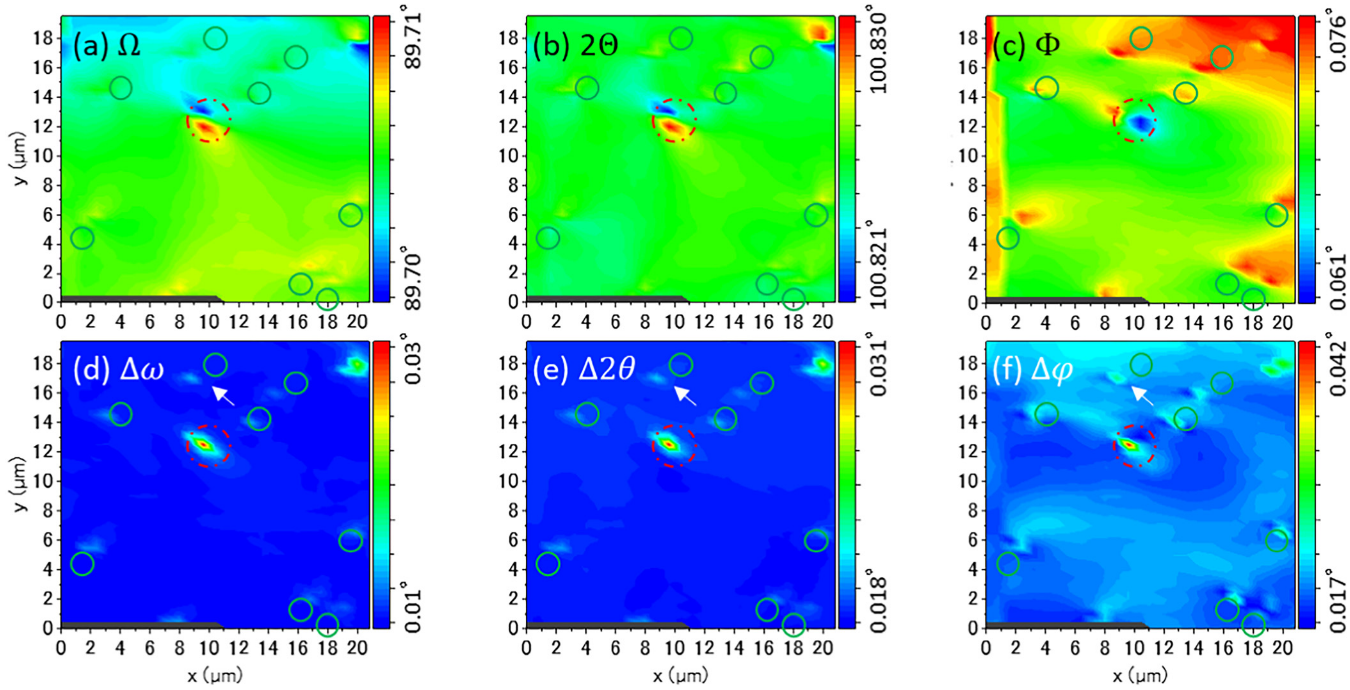

FIG. 3. Two-dimensional maps of Ω, 2Θ, Φ, $\Delta\omega$, $\Delta 2\theta$, and $\Delta\varphi$ in the area1 calculated from ω–2θ–φ mapping data. The circles indicating TD spots as described in Figs. 1(c) and 2(b) are superimposed.

fluctuations, which might be due to experimental errors since measured strains are close to the detection limit of our experiments, though fluctuations in the crystal possibly affect the strain field distribution. The highest values of $\Delta\omega$, $\Delta 2\theta$, and $\Delta\varphi$ for the typical XS-pits (indicated by an arrow in the maps) are 0.014°, 0.021°, and 0.026°, whereas for the L-pit, 0.027°, 0.030°, and 0.042°, suggesting that the mixed TD produces larger strain in the lattice structure than edge TDs. Figures 4(a)–4(f) present Ω, 2Θ, Φ, $\Delta\omega$, $\Delta 2\theta$, and $\Delta\varphi$ in the area2, including the M- and XS-pits, respectively. Two strained regions clearly seen in all the maps coincided with the M- and XS-pit. The highest values of $\Delta\omega$, $\Delta 2\theta$, and $\Delta\varphi$ at the M-pit region are 0.026°, 0.030°, and 0.038°, whereas at the XS-pit region, 0.015°, 0.022°, and 0.025°. Again, edge TDs are shown to generate smaller strain fields than screw TDs. These results demonstrated that the strain field around not only the edge and mixed TDs but also pure screw TDs having only the ***c***-component Burgers vector could be successfully identified by using the present nanoXRD technique.

The reciprocal lattice point at a specific measurement point, $\boldsymbol{Q}^p$, can be calculated based on the ω–2θ–φ data as follows:

$$\boldsymbol{Q}^p = \begin{pmatrix} Q_x^p \\ Q_y^p \\ Q_z^p \end{pmatrix} = \begin{pmatrix} \frac{1}{\lambda_0}\{-\cos\Omega_c^p + \cos\Phi^p\cos(2\Theta^p - \Omega_c^p)\} \\ \frac{1}{\lambda_0}\sin\Phi^p \\ \frac{1}{\lambda_0}\{\sin\Omega_c^p + \cos\Phi^p\sin(2\Theta^p - \Omega_c^p)\} \end{pmatrix}. \quad (1)$$

Here, $2\Theta^p$ and Φ^p are measured values of 2Θ and Φ at the specific measurement point, respectively. Ω_c^p was calculated as $\Omega^p - \alpha^p$, where Ω^p is a measured value of Ω and α^p is an offset angle of the (0001) plane in the $[11\bar{2}0]$ direction with respect to the sample surface at the respective measurement point. The α^p values were calculated by $2\Theta^{p,sym}/2 - \Omega^{p,sym}$ with the 0004 symmetric Bragg reflection dataset ($\Omega^{p,sym}$, $2\Theta^{p,sym}$) measured at the same points as for the $11\bar{2}4$ asymmetric reflection measurement. λ_0 is the wavelength of the incident x rays, which is 0.15498 nm. Respective average values of Ω_c^p, $2\Theta^p$, and Φ^p at all measurement points (referred to as $\overline{\Omega_c^p}$, $\overline{2\Theta^p}$, and $\overline{\Phi^p}$) in each measurement area, i.e., area1 and area2, were calculated to determine an average $11\bar{2}4$ reciprocal lattice point, $\bar{\boldsymbol{Q}}$, for the respective measurement areas by substituting the average values of ($\overline{\Omega_c^p}$, $\overline{2\Theta^p}$, $\overline{\Phi^p}$) for (Ω_c^p, $2\Theta^p$, Φ^p) in Eq. (1),

$$\bar{\boldsymbol{Q}} = \begin{pmatrix} Q_x \\ Q_y \\ Q_z \end{pmatrix} = \begin{pmatrix} \frac{1}{\lambda_0}\left\{-\cos\overline{\Omega_c^p} + \cos\overline{\Phi^p}\cos\left(\overline{2\Theta^p} - \overline{\Omega_c^p}\right)\right\} \\ \frac{1}{\lambda_0}\sin\overline{\Phi^p} \\ \frac{1}{\lambda_0}\left\{\sin\overline{\Omega_c^p} + \cos\overline{\Phi^p}\sin\left(\overline{2\Theta^p} - \overline{\Omega_c^p}\right)\right\} \end{pmatrix}. \quad (2)$$

Figure 5 schematically shows the relationship among $\boldsymbol{Q}^p$, $\bar{\boldsymbol{Q}}$ and strain components of ε_{ij}. The normal strain components of ε_{11}, ε_{22}, ε_{33} along the *a*-, *m*-, and *c*-axis are equivalent to the

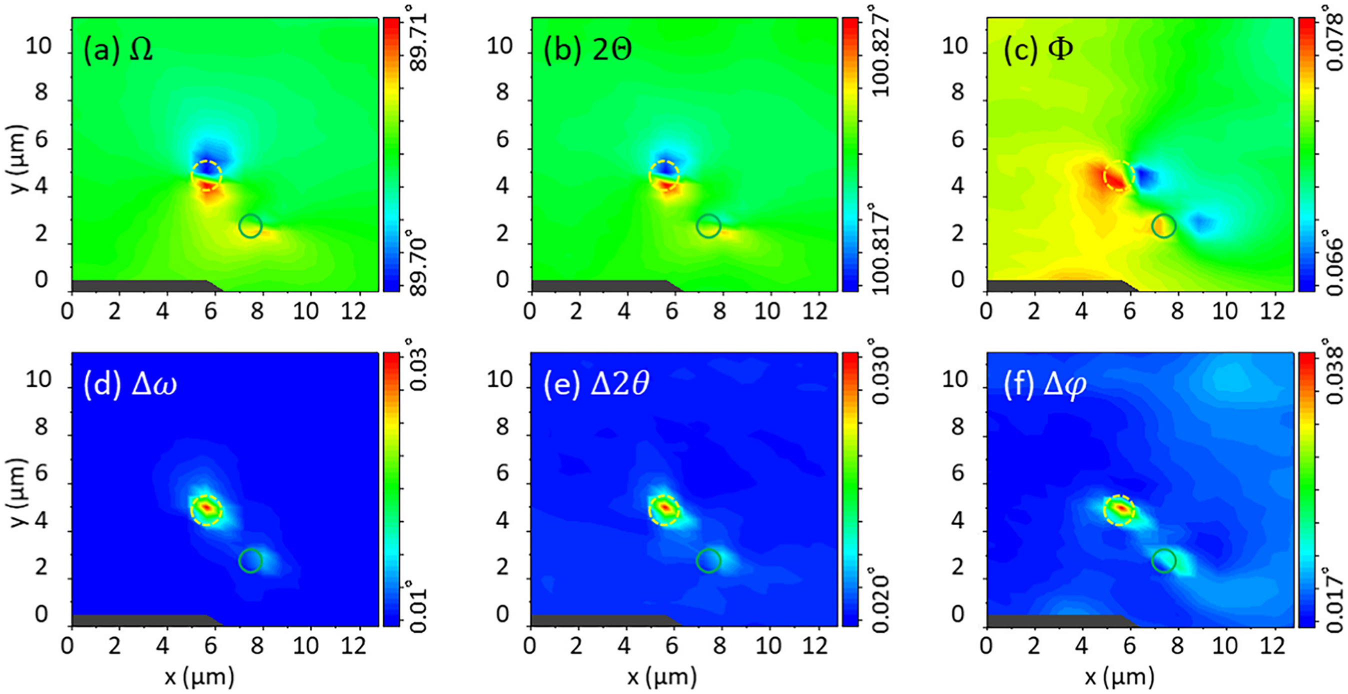

FIG. 4. Two-dimensional maps of Ω, 2Θ, Φ, Δω, Δ2θ, and Δφ in the area2 calculated from ω–2θ–φ mapping data. The circles indicating TD spots as described in Figs. 1(d) and 2(c) are superimposed.

differences in the q_x-, q_y-, and q_z-axis components of $\boldsymbol{Q}^p$ and $\bar{\boldsymbol{Q}}$, respectively, while the shear strain components of ε_{12} (or ε_{21}), ε_{23} (or ε_{32}), and ε_{13} (or ε_{31}) are equivalent to the angles between $\boldsymbol{Q}^p$ and $\bar{\boldsymbol{Q}}$ in the q_x–q_y, q_y–q_z, and q_z–q_x planes, respectively. Therefore, these strain tensor components can be experimentally obtained by the following equations:

$$\begin{pmatrix} \varepsilon_{11} & \varepsilon_{12} & \varepsilon_{13} \\ \varepsilon_{21} & \varepsilon_{22} & \varepsilon_{23} \\ \varepsilon_{31} & \varepsilon_{32} & \varepsilon_{33} \end{pmatrix} = \begin{pmatrix} \frac{\overline{Q_x}}{Q_x^p} - 1 & \frac{1}{2}\left\{\tan^{-1}\left(\frac{Q_y^p}{Q_x^p}\right) - \tan^{-1}\left(\frac{\overline{Q_y}}{\overline{Q_x}}\right)\right\} & \frac{1}{2}\left\{\tan^{-1}\left(\frac{Q_x^p}{Q_z^p}\right) - \tan^{-1}\left(\frac{\overline{Q_x}}{\overline{Q_z}}\right)\right\} \\ \frac{1}{2}\left\{\tan^{-1}\left(\frac{Q_y^p}{Q_x^p}\right) - \tan^{-1}\left(\frac{\overline{Q_y}}{\overline{Q_x}}\right)\right\} & \frac{\overline{Q_y}}{Q_y^p} - 1 & \frac{1}{2}\left\{\tan^{-1}\left(\frac{Q_z^p}{Q_y^p}\right) - \tan^{-1}\left(\frac{\overline{Q_z}}{\overline{Q_y}}\right)\right\} \\ \frac{1}{2}\left\{\tan^{-1}\left(\frac{Q_x^p}{Q_z^p}\right) - \tan^{-1}\left(\frac{\overline{Q_x}}{\overline{Q_z}}\right)\right\} & \frac{1}{2}\left\{\tan^{-1}\left(\frac{Q_z^p}{Q_y^p}\right) - \tan^{-1}\left(\frac{\overline{Q_z}}{\overline{Q_y}}\right)\right\} & \frac{\overline{Q_z}}{Q_z^p} - 1 \end{pmatrix}. \tag{3}$$

It should be noted that the normal strain component ε_{22} in the q_y-axis direction, or in the m-axis direction, cannot be calculated from these measurement data alone, because the present measurement setup is for $11\bar{2}4$ reflection parallel to the a-axis. Theoretically, the edge component of dislocations generates normal strains of ε_{11}, ε_{22} and shear strains of ε_{12} (or ε_{21}), whereas the screw component causes shear strains of ε_{13} (or ε_{31}) and ε_{23} (or ε_{32}). In this study, ε_{11} and ε_{12} were calculated for the XS-pit TD, while ε_{13} and ε_{23} for the M-pit TD. For the L-pit TD, both strain fields related to the edge and screw dislocation components were analyzed.

Figures 6(a)–6(d) show the strain tensor component maps of ε_{11}, ε_{12}, ε_{13}, and ε_{23} for the L-pit in the area1, respectively. A symmetrically extended strained area around the TD position (indicated by circles) was clearly seen in all the maps. According to the isotropic theory described in the supplementary material, the shear strains of ε_{13} and ε_{23} related to the screw dislocation with $\mathbf{b} = \langle 0001 \rangle$ can generate two patterns of strain fields depending on

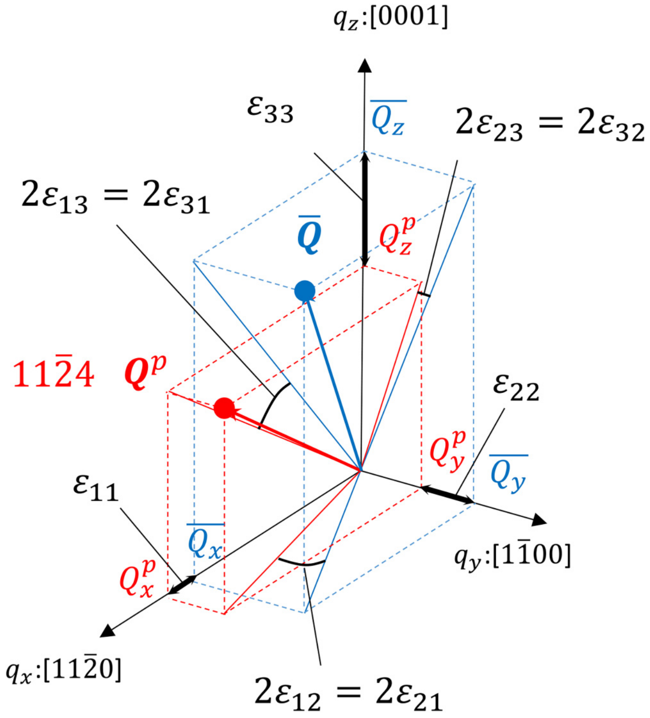

FIG. 5. The relationship between Q^p, $\bar{Q}$ and strain components of ε_{ij} schematically described in reciprocal space.

the sign of the Burges vector, as presented in Figs. S3(a) and S3(b), in the supplementary material, respectively. Comparison of the simulation and experimental results revealed that both strain components were in good agreements with the simulated ones related to $\mathbf{b} = [0001]$ rather than $\mathbf{b} = [000\bar{1}]$. The simulation results of ε_{13} and ε_{23} using $\mathbf{b} = [0001]$ are shown in Figs. 6(g) and 6(h). We observe generally good agreements between the experimental and theoretical strain distribution of the screw components (matching in the strain field direction may be obtained by rotating the simulation results slightly in the clockwise since a screw dislocation has rotational symmetry about the dislocation line). On the other hand, the TD having the edge dislocation component in the Burgers vector, such as $\mathbf{b} = 1/3\langle 11\bar{2}0\rangle = 1\boldsymbol{a}$ and $\mathbf{b} = \langle 1\bar{1}00\rangle = 1\,\boldsymbol{m}$, can theoretically generate six patterns of the strain fields of ε_{11} and ε_{12} depending on the direction of the Burgers vector, as presented in Figs. S1 and S2 of the supplementary material. For the L-pit TD estimated to have the $1\,\boldsymbol{m}$ component in the Burgers vector, the simulation results using $\mathbf{b} = [\bar{1}010]$, presented in Figs. 6(e) and 6(f), are in best agreement with both experimental results of ε_{11} and ε_{12}. Figures 7(a) and 7(b) present strain fields of ε_{13} and ε_{23} analyzed from the data around the M-pit estimated to have $\mathbf{b} = \langle 0001\rangle$ in the area2. Similarly, the symmetric strain centered on the TD position was observed. The Burgers vector of this M-pit TD was estimated to be $\mathbf{b} = [0001]$ based on the analogy between experimental and simulation results of ε_{13} and ε_{23}. Figures 8(a) and 8(b) show ε_{11} and ε_{12} maps around the XS-pit in area1. It was found that the magnitude of the strain of ε_{11} and ε_{12} around the XS-pit was comparably smaller than those around the L-pit in Figs. 6(a) and 6(b), indicating a difference in the magnitude of the

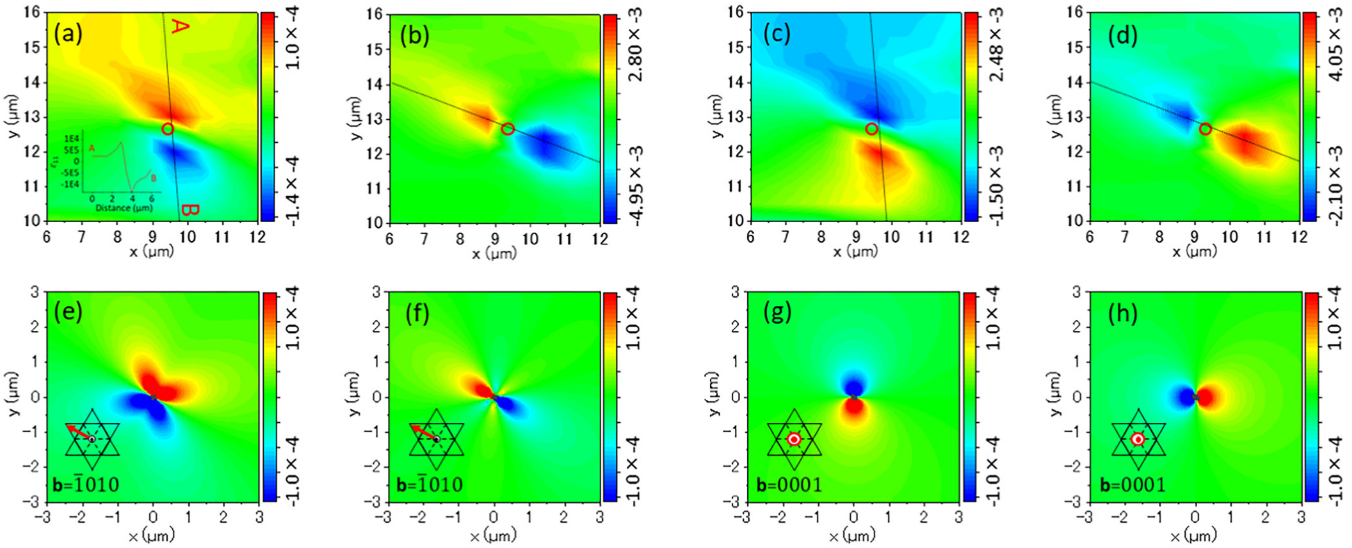

FIG. 6. The experimental strain tensor component maps of (a) ε_{11}, (b) ε_{12}, (c) ε_{13}, and (d) ε_{23} for the L-pit observed in the area1. In (a)–(d), the TD positions are indicated by red circles. The simulation results of (e) ε_{11} and (f) ε_{12} for the edge dislocation component of $\mathbf{b} = [\bar{1}010]$ and of (g) ε_{13} and (h) ε_{23} for the screw dislocation component of $\mathbf{b} = [0001]$.

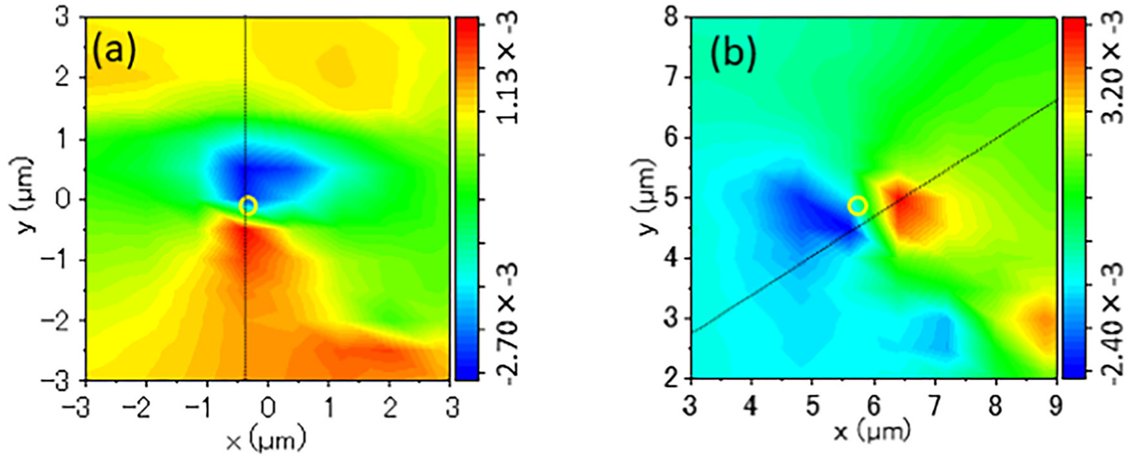

FIG. 7. The experimental strain tensor component maps of (a) ε_{13} and (b) ε_{23} for the M-pit observed in the area2. The TD positions are indicated by yellow circles.

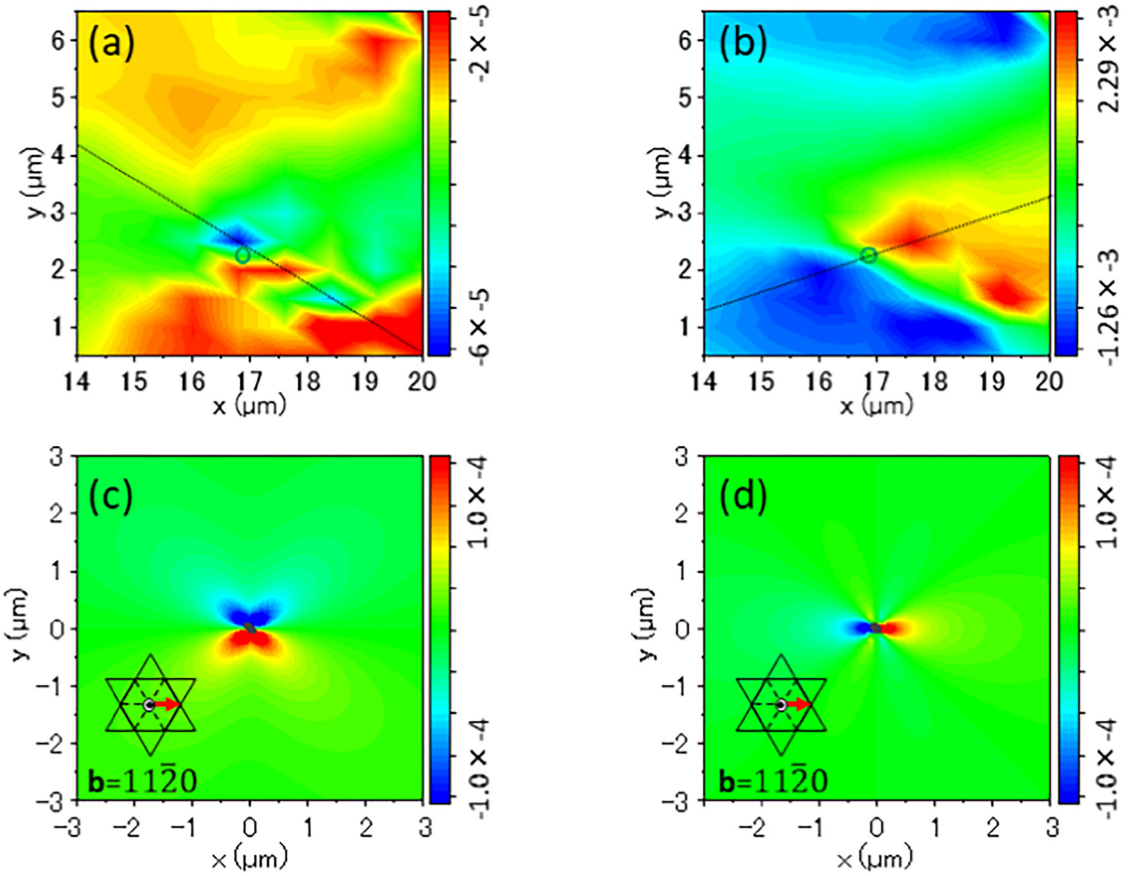

FIG. 8. The experimental strain tensor component maps of (a) ε_{11} and (b) ε_{12} for the XS-pit observed in the area1. In (a) and (b), the TD positions are indicated by green circles. The simulation results of (c) ε_{11} and (d) ε_{12} for the edge dislocation component of **b** = [11$\bar{2}$0].

in-plane component of the Burgers vector, as discussed later. As mentioned earlier, the edge component associated with $\mathbf{b} = 1\boldsymbol{a}$ can theoretically generate six patterns of ε_{11} and ε_{12} depending on the direction of the Burgers vector. Comparison of both the experimental results of ε_{11} and ε_{12} with the respective simulation ones indicated that the Burgers vector of this XS-pit TD was most likely $\mathbf{b} = 1/3[11\bar{2}0]$.

Finally, we attempt to discuss magnitude of the respective strain fields of the edge, screw, and mixed TDs. To compare the magnitude of strain fields, we tentatively adopted the strain change as evaluated from the difference between the highest and lowest values of strains measured by nanoXRD. Results of strain changes around the XS-, M-, and L-pit TDs and the ratio of the values for the L-pit TD to those for the XS- and M-pit TDs are summarized in Table S1 of the supplementary material. The results show that ε_{13} and ε_{23} for the L-pit TDs were 1.1 times larger than those for the M-pit TDs, indicating that the strain field of the screw dislocation component for the L- and M-pits was almost identical. On the other hand, the degrees of ε_{11} and ε_{12} for the L-pit TD were 5.9 and 2.0 times larger than those for the XS-pit TDs, respectively. The theoretical strain tensor component based on the elastic theory is proportional to the Burgers vector. Since the screw component of the Burges vector of the TD for the L-pit is estimated to be the same as the one for the M-pit ($\mathbf{b} = [0001]$), the theoretical ratios of ε_{13} and ε_{23} values of L-pit TD to those of M-pit TD were both 1.0. Thus, the experimental results of the strain change related to the screw component showed good agreement with the elastic theory. In the case of the edge component of the L-pit TD with $\mathbf{b} = 1\,\boldsymbol{m}$, on the other hand, it should produce 1.7 times larger strain of ε_{11} and ε_{12} than that of the XS-pit TD with $\mathbf{b} = 1\boldsymbol{a}$ according to the theory. The experimental ratios of the strain shift for ε_{11} and ε_{12} around the L-pit TD to the XS-pit TD were larger than those expected from the elastic theory. These discrepancies may be attributed to the limitation of spatial resolution in the current nanoXRD experiments. In the simple elastic theory, strain divergently increases at the dislocation core region of the nm scale, so some threshold radius for the core has to be introduced to define the peak strain. The present nanoXRD experiments measured strains averaged over x-ray beam irradiation volume ($\approx 3\,\mu\mathrm{m}^3$) and the precise evaluation of peak strain is hindered by a small volume ratio of the core region and dependency on sampling probe positions. This is in contrast to HRTEM based GPA, which observes percent order strain at the nm scale region near the dislocation core. Nevertheless, the present measurements capture the shapes of extended strain fields that are similar to those predicted from the elastic theory as seen in Fig. 6. Also, recent progress of the x-ray mirror optical system enables focusing of the x-ray beam down to around 10 nm.[30,31] Improvements in spatial resolution due to reduced x-ray beam size in conjunction with 10^{-4} strain sensitivity will provide further opportunities for non-destructive analysis of three-dimensional strain tensor fields in crystals.

IV. CONCLUSION

This study demonstrated that position-dependent three-dimensional RSM using nanoXRD sensitively detect variation in the microlattice structure around all types of individual TDs in the GaN bulk crystal, i.e., the edge TDs with $\mathbf{b} = 1/3\langle 11\bar{2}0\rangle = 1\boldsymbol{a}$, the screw TDs with $\mathbf{b} = <0001> = 1\boldsymbol{c}$, and the mixed TDs with $\mathbf{b} = \langle 1\bar{1}01\rangle = 1\boldsymbol{m} + 1\boldsymbol{c}$. The strain fields corresponding to the respective strain tensor components around each TD were analyzed using the three-dimensional RSM data. The strain fields showing a nearly symmetrical strained region centered on the respective TD positions were in good agreements with the simulation results based on the isotropic elastic theory with a particular Burgers vector. The magnitude of the shear strain tensor components associated with the screw dislocation component, ε_{13} and ε_{23} of the mixed TD with $\mathbf{b} = 1\boldsymbol{m} + 1\boldsymbol{c}$ and the screw TD with $\mathbf{b} = 1\boldsymbol{c}$, was almost the same, which was reasonably consistent with the isotropic elastic theory. On the other hand, for the edge dislocation related strain components, ε_{11} and ε_{12}, the ratios of the strain shift around the mixed TD with $\mathbf{b} = 1\boldsymbol{m} + 1\boldsymbol{c}$ to the edge TD with $\mathbf{b} = 1\boldsymbol{a}$, were larger than the theoretical values expected from the isotropic elastic model. Several inconsistencies between the experimental and theoretical strains in quantitative aspects may be attributed to the limitation in the spatial resolution of the current experiments, and further improvements are issues in future work. The present method is particularly beneficial in that it allows non-destructive analysis of screw components of TDs that tend to contribute to leakage characteristics and are not routinely accessible by other conventional analysis methods. These results indicate that nanoXRD could be a powerful way to reveal three-dimensional strain fields associated with arbitrary types of TDs in semiconductor materials, such as GaN and SiC.

SUPPLEMENTARY MATERIAL

Additional simulation results of strain tensor components of edge and screw dislocations based on the isotropic elastic theory and results of strain change at TDs are included in the supplementary material.

ACKNOWLEDGMENTS

The nanoXRD measurement was performed at BL13XU at SPring-8 with the approval of JASRI (Proposal Nos. 2019B1797, 2019B2101, 2020A1136, 2020A1331, 2020A1402, 2020A1652, 2021A1207, 2021A1584, 2021B1345, 2021B1650, 2022B1567, 2022B1817, 2023A1695, and 2023A3599). The authors gratefully acknowledge funding from the Japan Science and Technology Agency (Project No. J121052565). A part of this work was also supported by a Kakenhi Grant-in-Aid (No. JP16H06423) and Murata Science and Education Foundation.

AUTHOR DECLARATIONS

Conflict of Interest

The authors have no conflicts to disclose.

Author Contributions

T. Hamachi: Conceptualization (equal); Investigation (lead); Methodology (equal); Writing – original draft (lead); Writing – review & editing (equal). **T. Tohei:** Conceptualization (equal); Investigation (equal); Methodology (equal); Supervision (equal);

Writing – original draft (equal); Writing – review & editing (equal). **Y. Hayashi:** Investigation (supporting); Methodology (supporting); Writing – original draft (supporting); Writing – review & editing (supporting). **S. Usami:** Resources (supporting). **M. Imanishi:** Resources (supporting). **Y. Mori:** Resources (equal). **K. Sumitani:** Methodology (supporting); Resources (supporting). **Y. Imai:** Methodology (supporting); Resources (supporting). **S. Kimura:** Methodology (supporting); Resources (supporting). **A Sakai:** Conceptualization (equal); Funding acquisition (lead); Investigation (equal); Methodology (equal); Project administration (lead); Resources (equal); Supervision (lead); Writing – original draft (equal); Writing – review & editing (equal).

DATA AVAILABILITY

The data that support the findings of this study are available from the corresponding author upon reasonable request.

REFERENCES

[1] T. Oka, Jpn. J. Appl. Phys. **58**, SB0805 (2019).
[2] T. Kachi, Jpn. J. Appl. Phys. **53**, 100210 (2014).
[3] X. She, A. Q. Huang, O Lucia, and B. Ozpineci, IEEE Trans. Ind. Electron. **64**, 8193 (2017).
[4] J. Biela, M. Schweizer, S. Waffler, and J. W. Kolar, IEEE Trans. Ind. Electron. **58**, 2872 (2011).
[5] H. Ohta, N. Asai, F. Horikiri, Y. Narita, T. Yoshida, and T. Mishima, Jpn. J. Appl. Phys. **60**, SBBD09 (2021).
[6] S. Usami, Y. Ando, A. Tanaka, K. Nagamatsu, M. Deki, M. Kushimoto, S. Nitta, Y. Honda, H. Amano, Y. Sugawara, Y.-Z. Yao, and Y. Ishikawa, Appl. Phys. Lett. **112**, 182106 (2018).
[7] K. Konishi, Y. Nakamura, A. Nagae, N. Kawabata, T. Tanaka, N. Tomita, H. Watanabe, S. Tomohisa, and N. Miura, Jpn. J. Appl. Phys. **59**, 011001 (2020).
[8] T. Narita, M. Kanechika, J. Kojima, H. Watanabe, T. Kondo, T. Uesugi, S. Yamaguchi, Y. Kimoto, K. Tomita, Y. Nagasato, S. Ikeda, M. Kosaki, T. Oka, and J. Suda, Sci. Rep. **12**, 1458 (2022).
[9] D. C. Look and J. R. Sizelove, Phys. Rev. Lett. **82**, 1237 (1999).
[10] M. Țapajna, S. W. Kaun, M. H. Wong, F. Gao, T. Palacios, U. K. Mishra, J. S. Speck, and M. Kuball, Appl. Phys. Lett. **99**, 223501 (2011).
[11] I. Arslan and N. D. Browning, Phys. Rev. Lett. **91**, 165501 (2003).
[12] T. Nakano, Y. Harashima, K. Chokawa, K. Shiraishi, A. Oshiyama, Y. Kangawa, S. Usami, N. Mayama, K. Toda, A. Tanaka, Y. Honda, and H. Amano, Appl. Phys. Lett. **117**, 012105 (2020).
[13] S. K. Rhode, M. K. Horton, M. J. Kappers, S. Zhang, C. J. Humphreys, R. O. Dusane, S. L. Sahonta, and M. A. Moram, Phys. Rev. Lett. **111**, 025502 (2013).
[14] M. Garbrecht, B. Saha, J. L. Schroeder, L. Hultman, and T. D. Sands, Sci. Rep. **7**, 46092 (2017).
[15] Y. Yao, Y. Sugawara, D. Yokoe, K. Sato, Y. Ishikawa, N. Okada, K. Tadatomo, M. Sudo, M. Kato, M. Miyoshi, and T. Egawa, CrystEngComm **22**, 8299 (2020).
[16] T. Hamachi, T. Tohei, Y. Hayashi, M. Imanishi, S. Usami, Y. Mori, N. Ikarashi, and A. Sakai, J. Appl. Phys. **129**, 225701 (2021).
[17] S. Onda, H. Watanabe, Y. Kito, H. Kondo, H. Uehigashi, N. Hosokawa, Y. Hisada, K. Shiraishi, and H. Saka, Philos. Mag. Lett. **93**, 439 (2013).
[18] S. Onda, H. Watanabe, T. I. Okamoto, H. Kondo, H. Uehigashi, and H. Saka, Philos. Mag. Lett. **95**, 489 (2015).
[19] M. J. Hÿtch, J.-L. Putaux, and J.-M. Pénisson, Nature **423**, 270 (2003).
[20] N. Kokubo, Y. Tsunooka, F. Fujie, J. Ohara, S. Onda, H. Yamada, M. Shimizu, S. Harada, M. Tagawa, and T. Ujihara, Jpn. J. Appl. Phys. **58**, SCCB06 (2019).
[21] N. Kokubo, Y. Tsunooka, F. Fujie, J. Ohara, S. Onda, H. Yamada, M. Shimizu, S. Harada, M. Tagawa, and T. Ujihara, Appl. Phys. Exp. **11**, 111001 (2018).
[22] S. Sintonen, M. Rudziński, S. Suihkonen, H. Jussila, M. Knetzger, E. Meissner, A. Danilewsky, T. O. Tuomi, and H. Lipsanen, J. Appl. Phys. **116**, 083504 (2014).
[23] T. Ohno, H. Yamaguchi, S. Kuroda, K. Kojima, T. Suzuki, and K. Arai, J. Cryst. Growth **260**, 209 (2004).
[24] S. Kamada, S. Takeuchi, D. T. Khan, H. Miyake, K. Hiramatsu, Y. Imai, S. Kimura, and A. Sakai, Appl. Phys. Express **9**, 111001 (2016).
[25] K. Shida, N. Yamamoto, T. Tohei, M. Imanishi, Y. Mori, K. Sumitani, Y. Imai, S. Kimura, and A. Sakai, Jpn. J. Appl. Phys. **58**, SCCB16 (2019).
[26] K. Shida, S. Takeuchi, T. Tohei, Y. Imai, S. Kimura, A. Schulze, M. Caymax, and A. Sakai, Semicond. Sci. Technol. **33**, 124005 (2018).
[27] W. Takeuchi, E. Kagoshima, K. Sumitani, Y. Imai, S. Shibayama, M. Sakashita, S. Kimura, H. Tomita, T. Nishiwaki, H. Fujiwara, and O. Nakatsuka, Jpn. J. Appl. Phys. **61**, SC1072 (2022).
[28] Y. Mori, M. Imanishi, K. Murakami, and M. Yoshimura, Jpn. J. Appl. Phys. **58**, SC0803 (2019).
[29] Y. Imai, S. Kimura, D. Kan, and Y. Shimakawa, AIP Conf. Proc. **1741**, 050014 (2016).
[30] J. Yamada, S. Matsuyama, R. Hirose, Y. Takeda, Y. Kohmura, M. Yabashi, K. Omote, T. Ishikawa, and K. Yamauchi, Optica **7**, 367 (2020).
[31] T. Inoue, S. Matsuyama, J. Yamada, N. Nakamura, T. Osaka, I. Inoue, Y. Inubushi, K. Tono, H. Yumoto, T. Koyama, H. Ohashi, M. Yabashi, T. Ishikawa, and K. Yamauchi, J. Synchrotron Rad. **27**, 883 (2020).